

Spin-bias-controlled current rectification and negative magnetoresistance in a quantum dot spin transistor

Zhengzhong Zhang(张正中), Han Hu(胡涵), Runze Zhu(朱润泽), Yanzong Wang(王延宗), and Hao Liu(刘昊)
Citation: Chin. Phys. B, 2026, 35 (**7**): 077202. DOI: 10.1088/1674-1056/ae1017
http://cpb.iphy.ac.cn; http://iopscience.iop.org/cpb

What follows is a list of articles you may be interested in

Large Seebeck coefficient resulting from chiral interactions in triangular triple quantum dots

Yi-Ming Liu(刘一铭) and Jian-Hua Wei(魏建华)
Chin. Phys. B, 2022, 31 (**9**): 097201. DOI: 10.1088/1674-1056/ac6dae

Chiral splitting of Kondo peak in triangular triple quantum dot

Yi-Ming Liu(刘一铭), Yuan-Dong Wang(王援东), and Jian-Hua Wei(魏建华)
Chin. Phys. B, 2022, 31 (**5**): 057201. DOI: 10.1088/1674-1056/ac29a5

Capacitive coupling induced Kondo-Fano interference in side-coupled double quantum dots

Fu-Li Sun(孙复莉), Yuan-Dong Wang(王援东), Jian-Hua Wei(魏建华), Yi-Jing Yan(严以京)
Chin. Phys. B, 2020, 29 (**6**): 067204. DOI: 10.1088/1674-1056/ab8ac1

Electrically tunable spin diode effect in a tunneling junction of quantum dot

Xukai Peng(彭许凯), Zhengzhong Zhang(张正中)
Chin. Phys. B, 2019, 28 (**12**): 127202. DOI: 10.1088/1674-1056/ab53d0

Magnetotransport properties of graphene layers decorated with colloid quantum dots

Ri-Jia Zhu(朱日佳), Yu-Qing Huang(黄雨青), Jia-Yu Li(李佳玉), Ning Kang(康宁), Hong-Qi Xu(徐洪起)
Chin. Phys. B, 2019, 28 (**6**): 067201. DOI: 10.1088/1674-1056/28/6/067201

Spin-bias-controlled current rectification and negative magnetoresistance in a quantum dot spin transistor

Zhengzhong Zhang(张正中)[†], Han Hu(胡涵), Runze Zhu(朱润泽), Yanzong Wang(王延宗), and Hao Liu(刘昊)[‡]

Faculty of Mathematics and Physics, Huai'an University, Huai'an 223003, *China*

(Received 9 July 2025; revised manuscript received 12 September 2025; accepted manuscript online 7 October 2025)

We propose a spin-bias-controlled quantum-dot spin-valve device and systematically investigate its charge and spin transport properties. Numerical results reveal that the parallel magnetic configuration enables gate-tunable rectification of both charge and spin currents, whereas no rectification occurs in the antiparallel configuration. Remarkably, in specific gate voltage regimes, the device achieves perfect charge rectification — characterized by complete suppression of reverse-bias charge currents — while sustaining finite spin currents. Furthermore, a negative magnetoresistance emerges in this system, electrically tunable to its theoretical minimum of -1, accompanied by an antiparallel to parallel current on/off ratio exceeding 10^6. This behavior implies that within tailored gate voltage regimes, only the antiparallel configuration permits charge conduction, with electron current entirely blocked in the parallel configuration. These results establish spin-bias-driven quantum dot systems as multifunctional platforms for tunable rectification and magnetoresistance control, highlighting their potential for advancing spintronic technologies.

Keywords: quantum dot, spin diode, spin valve

PACS: 72.25.–b, 72.25.Dc, 72.25.Hg, 73.21.La

DOI: 10.1088/1674-1056/ae1017 **CSTR:** 32038.14.CPB.ae1017

1. Introduction

Spintronics, a rapidly evolving field within condensed matter physics, utilizes electron spin as an alternative information carrier to charge, achieving revolutionary progress over the past three decades.[1,2] A series of fundamental phenomena including giant magnetoresistance (GMR), spin Hall effect, and spin–orbit torque have not only enriched our understanding of condensed matter systems but also catalyzed transformative technological applications.[3–5] Among these breakthroughs, magnetoresistive devices stand out as the most successful physical invention in spintronics history. To date, large-scale implementations of GMR-based read heads and tunnel magnetoresistance (TMR) memory units have achieved ubiquitous presence in commercial electronics, ranging from high-density hard disk drives to emerging magnetic random-access memory architectures.[6–8] This remarkable commercialization success has been accompanied by continuous theoretical advancements. Novel device concepts exploiting the spin degree of freedom, including spin valves, spin-transfer torque memory, pure spin current generators, and spin-caloritronic devices, have demonstrated extraordinary potential in laboratory settings.[9–15] Particularly, spin current generators and spin diodes have shown exceptional performance metrics in prototype demonstrations.[16–24] These parallel developments not only reaffirm spintronics' transformative power in fundamental science but also establish a robust technological pathway toward energy-efficient, non-volatile, and ultra-fast computing systems for the post-Moore's law era.[25]

The operational paradigm of conventional electronic circuits is fundamentally rooted in electrical bias and current-driven charge transport mechanisms. However, with the rapid advancements in spintronics and materials science, numerous materials and circuit architectures have recently been demonstrated to generate spin bias or pure spin currents.[26–29] Unlike traditional electrical bias, devices driven by spin bias exhibit a dominant role of spin transport over charge transport. Leveraging this unique characteristic, a range of innovative spin-bias-controlled electronic devices, such as spin current diodes, spin qubits, and spin-orbital angular momentum memory cells, have emerged, all of which depend on the manipulation of spin bias or spin currents.[30–38] In these systems, the driving mechanism for device functionality shifts from charge transport to spin transport, significantly reducing Joule heating effects. Furthermore, by coupling quantum dots[39,40] (QDs) or constructing heterostructures, spin bias can be converted into conventional electrical bias to drive charge transport.[41–44] These discoveries position spin bias as a cornerstone control mechanism in contemporary spintronics, while advancing innovative architectural paradigms for future ultra-efficient elec-

[†]Corresponding author. E-mail: zeikeezhang@163.com

[‡]Corresponding author. E-mail: hyitliuh@163.com

© 2026 Chinese Physical Society and IOP Publishing Ltd. All rights, including for text and data mining, AI training, and similar technologies, are reserved.

tronic systems.

2. Concept

Recently, the experimental observation of non-local spin-bias signals in silicon and graphene nanowires has been reported.[45–47] This discovery has inspired innovative device architectures, including QD-based spin qubits and spin valve configurations.[48–50] The synergistic interplay between spin and charge biases in these systems is predicted to enhance thermal stability significantly, particularly manifesting an extraordinary switching ratio between antiparallel currents (J_{AP}) and parallel (J_P) currents in devices, where on-off ratios J_{AP}/J_P can attain values as high as 10^6. This phenomenon stands in stark contrast to conventional TMR effects where antiparallel currents are generally suppressed compared to parallel currents. The observed anomalous switching ratio implies near-total suppression of parallel currents, corresponding to the emergence of a pronounced negative magnetoresistance[51–53] (NMR) effect. Inspired by these advancements, we propose and theoretically investigate a QD-based spin valve device driven by spin bias in this work. As shown in Figs. 1(a) and 1(b), our configuration comprises two low-dimensional ferromagnetic electrode layers weakly coupled to a central QD, where a spin injector induces spin accumulation on the source (S) lead. According to recent experimental data,[56,57] this method enables the generation of spin-resolved electrochemical potential differences as high as approximately 4 meV in Si- or graphene-based nanoscale thin films at room temperature. If the conductive layer is nonmagnetic, the spin-resolved density of states near the Fermi level in the electrodes remains symmetric, with only distinct electrochemical potential distributions in the leads; however, for ferromagnetic layers, the spin bias creates an electrochemical potential difference between spin majority and minority carriers (as shown in Fig. 1(c)). Figure 1(d) schematically depicts the conductive channels in the electrodes and the energy levels of the QD in the device. The energy levels within the QD can be modulated by the gate voltage, while the electrochemical potentials in the source electrode can be controlled by the spin bias V_S, satisfying $\mu_\uparrow^S = -\mu_\downarrow^S = eV_S$.

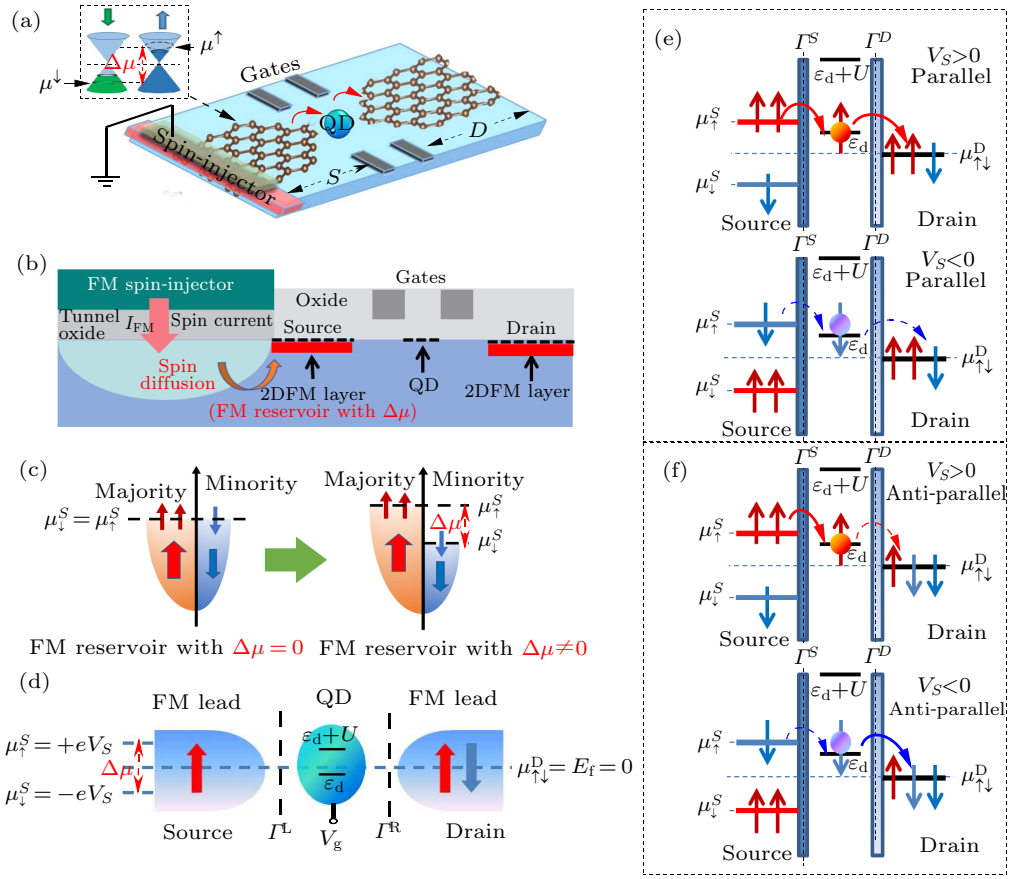


Fig. 1. Schematic diagrams of the spin-bias-driven device structure in (a) top view and (b) side view. The device comprises a pair of nanoscale ferromagnetic electrode layers (*e.g.*, magnetically doped graphene or silicene[54,55]) coupled to a gate-voltage-tunable QD. The QD is isolated from source and drain electrodes through tunnel barriers. In the source ferromagnetic layer, external spin injection induces spin accumulation ($\Delta\mu$), generating a spin bias. The magnitude and direction of this spin bias can be controlled by the drive current I_{FM}. (c) Comparative schematic diagram illustrates the contrast in carrier electrochemical potential distributions and spin-resolved density of states profiles within ferromagnetic electrodes under (left) no spin bias ($\Delta\mu = 0$) and (right) spin bias ($\Delta\mu \neq 0$) configurations. (d) Schematic diagram of energy levels in the quantum dot and spin-resolved transport channels in the electrodes: The transport behavior of spin-dependent carriers in the leads can be modulated by the gate voltage through selective tuning of the electron transport channels within the quantum dot. Figures 1(e) and 1(f) show the electron transport under varying spin bias polarities in (e) parallel and (f) antiparallel configurations, where transport is dominated by the QD's single-occupied energy level ε_d.

Figures 1(e) and 1(f) illustrate the fundamental operating principles of the device. When the electrodes' magnetic orientations are parallel, a positive spin bias promotes dominant transport of spin-majority carriers from the source electrode to the drain (D) electrode, generating substantial charge and spin currents. Conversely, reversing the spin bias polarity induces transport dominated by spin-minority carriers, producing an inverted current response. This spin-polarity-dependent transport leads to marked asymmetries in both charge and spin distributions within the device, constituting a distinct spin diode effect. Crucially, such asymmetries are absent in antiparallel magnetic configurations. This occurs because, in antiparallel structures, electrons traversing the QD always act as majority spins in one electrode while simultaneously being minority spins in the other. Consequently, the system's current is no longer dominated by spin-minority carriers, and thus the current suppression is incomplete.

Additionally, the current rectification effect in parallel configurations results in the dependence of the device's magnetoresistance on both the spin bias and gate voltage. By comparing Figs. 1(e) and 1(f), when the parallel-configuration device operates in the "forward" bias direction ($V_S > 0$), the spin-majority-dominated parallel current leads to a TMR ratio greater than zero. Conversely, in the "reverse" direction ($V_S < 0$), the spin-minority-dominated parallel current results in a TMR ratio less than zero, thereby giving rise to the NMR phenomenon. Interestingly, our numerical results in Section 4 demonstrate that even when using ferromagnetic electrodes with relatively low spin polarization, the device can consistently achieve an extremely high diode rectification ratio and a perfect negative magnetoresistance effect (TMR = -1) by adjusting the gate voltage to specific values. For the diode, this phenomenon corresponds to the complete suppression of reverse current. For the magnetoresistance device, TMR = -1 signifies the complete suppression of parallel current and an exceptionally high on-off ratio between antiparallel current and parallel current (*e.g.*, at a temperature of $T = 1$ K and a spin bias $|V_S| > 1.3$ mV, both the diode rectification ratio and the magnetoresistance on-off ratio can reach $\sim 10^6$).

Compared to the functional parameters of the diode and magnetoresistance devices shown in Table 1, although our design requires a lower operating temperature, it not only achieves an extremely high diode rectification ratio but also incorporates the functionality of a spin valve. Although the observed negative magnetoresistance effect exhibits superficial similarities to the phenomenon reported in Ref. [50], their underlying physical mechanisms are fundamentally distinct.

Table 1. Performance comparison of state-of-the-art diode and magnetic tunnel junction.[58–63]

Device structure	Rectification ratio	TMR (%)	Temperature (K)
Diodes			
Pt–MoS_2/graphene heterojunction	$\sim 10^6$	N/A	~300
PtNPs/TiO_2/Pt metal–insulator–metal diode	~ 50	N/A	~300
$CuCrP_2S_6$-based ferroelectric tunnel junction	$\sim 10^3$	N/A	~300
Magnetic tunnel junctions (MTJ)			
CoFeB/MgO/CoFeB MTJ	N/A	200–600	~300
Fe_3GaTe_2/InSe/Fe_3GaTe_2 MTJ	N/A	$\sim 10^6$	~300
Mn_3Ge Heusler alloys/MgO MTJ	N/A	~ 100	~300

TMR is not applicable (N/A) to non-magnetic diode devices.

3. Model and method

The Hamiltonian governing the quantum dot (QD) spin-valve system is expressed as[30,64]

$$H = H_{\text{leads}} + H_{\text{hyb}} + \sum_{\sigma} \varepsilon_d d_\sigma^\dagger d_\sigma + U d_\uparrow^\dagger d_\uparrow d_\downarrow^\dagger d_\downarrow, \tag{1}$$

where $H_{\text{leads}} = \sum_{\alpha k\sigma} \varepsilon_{\alpha k\sigma} c_{\alpha k\sigma}^\dagger c_{\alpha k\sigma}$ models the noninteracting ferromagnetic electrodes. Here, α ($\alpha \in \{S, D\}$) labels the source/drain leads, $\sigma = \uparrow (\downarrow)$ denotes spin, and $c_{\alpha k\sigma}^\dagger$ ($c_{\alpha k\sigma}$) is the creation (annihilation) operator for the electron of momentum k, spin σ and energy $\varepsilon_{\alpha k\sigma}$ in lead α. The tunneling Hamiltonian $H_{\text{hyb}} = \sum_{\alpha k\sigma} \left(t_\alpha c_{\alpha k\sigma}^\dagger d_\sigma + \text{h.c.} \right)$ describes the lead–dot couplings via spin- and momentum-independent hybridization strengths t_α. The QD is characterized by its gate-tunable level ε_{d}, intra-dot Coulomb repulsion U and electron creation (annihilation) operator $d_\sigma^\dagger$ (d_σ).

Due to weak QD–lead coupling, electron transport is dominated by sequential tunneling. When the hybridization-induced level broadening is smaller than the charging energy and temperatures exceed the Kondo temperature, the rate equations become valid.[65–67] The QD's occupation probabilities ρ_i evolve via a set of rate equations:

$$\frac{\mathrm{d}\rho_i}{\mathrm{d}t} = \sum_f \left(\rho_f \omega_{f\to i} - \rho_i \omega_{i\to f} \right), \tag{2}$$

where $i(f)$ corresponds to four possible states in QD, namely, the empty state $|0\rangle$, the spin-up electron occupied state $|\uparrow\rangle$, the spin-down electron occupied state $|\downarrow\rangle$, and the doubly occupied state $|\uparrow\downarrow\rangle$. Transition rates $\omega_{i\to f} = \Sigma_{\alpha\sigma}(\omega_{i\to f}^{\alpha\sigma+} + \omega_{i\to f}^{\alpha\sigma-})$ are derived via Fermi's golden rule:

$$\omega_{i\to f}^{\alpha\sigma+} = \Gamma_{\alpha\sigma} f_{\alpha\sigma}(\varepsilon_f - \varepsilon_i - \mu_\alpha^\sigma) |\langle f | d_\sigma^\dagger | i \rangle|^2,$$

$$\omega_{i\to f}^{\alpha\sigma-} = \Gamma_{\alpha\sigma} f_{\alpha\sigma}(\varepsilon_i - \varepsilon_f + \mu_\alpha^\sigma)|\langle f|d_\sigma|i\rangle|^2. \quad (3)$$

Here, $\Gamma_{\alpha\sigma} = 2\pi\wp_{\alpha\sigma}|t_\alpha|^2$ represents the linewidth function for lead α, where $\wp_{\alpha\sigma}$ denotes the spin-dependent density of states at the Fermi energy E_f. If we assume the linewidth function is energy-independent and consider symmetric coupling between QD and electrodes, the $\Gamma_{\alpha\sigma}$ can be simplified as $\Gamma_{\alpha\uparrow} = \Gamma_0(1+P_\alpha)$ and $\Gamma_{\alpha\downarrow} = \Gamma_0(1-P_\alpha)$, where $\Gamma_0 = (\Gamma_{\alpha\uparrow}+\Gamma_{\alpha\downarrow})/2$. Spin polarization P_α quantifies the asymmetry in the density of states for spin-up and spin-down electrons at the Fermi level in lead α, which can be defined as $P_\alpha = (\wp_{\alpha\uparrow} - \wp_{\alpha\downarrow})/(\wp_{\alpha\uparrow} + \wp_{\alpha\downarrow})$.

Since electron transport is driven by spin bias rather than electrical bias, following the definitions in Refs. [42,43], the spin splitting of the chemical potential in lead α is defined as $\Delta\mu^\alpha = (\mu_\uparrow^\alpha - \mu_\downarrow^\alpha)/2$, and the spin bias between two leads denoted as V_s, is given by $eV_s = \Delta\mu^S - \Delta\mu^D$. Given that there is no spin accumulation in the drain electrode, the spin-dependent electrochemical potentials in the electrodes are defined as $\mu_\uparrow^S = -\mu_\downarrow^S = eV_S$ and $\mu_\uparrow^D = -\mu_\downarrow^D = E_\mathrm{f} = 0$ (as illustrated in Fig. 1(d)). Here, μ_σ^α represents the chemical potential of spin-σ carriers in lead α, and their thermal distribution follows the Fermi–Dirac form:

$$f_{\alpha\sigma}(\varepsilon) = \left[\exp\left(\frac{\varepsilon - \mu_\sigma^\alpha}{k_\mathrm{B}T_\alpha}\right) + 1\right]^{-1},$$

where T_α denotes the temperature of lead α.

Finally, the steady-state solution of Eq. (2) can be obtained by the normalization condition $\sum_i \rho_i = 1$ and the equilibrium condition $\mathrm{d}\rho_i/\mathrm{d}t = 0$. Then the spin-$\sigma$ current in lead α can be calculated as

$$J_{\alpha\sigma} = -(e/h)\sum_{i,f}(n_i - n_f)\omega_{f\to i}^{\alpha\sigma}\rho_f, \quad (4)$$

where $n_{i(f)}$ is the number of electrons in state $i(f)$. The net spin-resolved currents through the QD are $J_\sigma = (J_{S\sigma} - J_{D\sigma})/2$, and the total charge ($J_C$) and spin ($J_S$) currents are expressed as: $J_{C/S} = J_\uparrow \pm J_\downarrow$, where "+" corresponds to J_C, and "−" to J_S. To evaluate the magnetoresistance, we consider two configurations of lead polarization: parallel ($P_S = P_D = \eta$) and antiparallel ($P_S = -P_D = \eta$). Then the TMR ratio is calculated by

$$\mathrm{TMR} = \frac{J_\mathrm{P} - J_\mathrm{AP}}{J_\mathrm{AP}}, \quad (5)$$

where J_P (J_AP) denotes the charge current in the parallel (antiparallel) magnetic configuration of the device.

4. Results and discussion

4.1. Tuning current spectrum via spin bias and gate voltage

In the following calculations, the charge and spin currents are scaled by $e\Gamma_0/\hbar$, and the Coulomb repulsion energy of the QD is set to $U = 7$ meV based on experimental parameters.[68] To ensure weak coupling between the dot and the leads, Γ_0 is typically set to ~ 0.01 meV.[50,66] The spin polarization $\eta \in (0,1)$ indicates that majority carriers in parallel magnetic configurations exhibit spin-up polarization. To systematically analyze the charge and spin currents under different spin bias polarities, we define $J_{C/S}^+$ and $J_{C/S}^-$ as the charge (or spin) currents under positive ($V_S > 0$) and negative ($V_S < 0$) spin bias, respectively. Figure 2 illustrates the distribution of charge and spin current as functions of gate voltage and spin bias for both parallel (Figs. 2(a) and 2(c)) and antiparallel (Figs. 2(b) and 2(d)) configurations. Consistent with the theoretical predictions in Fig. 1, the parallel configuration exhibits pronounced asymmetric distributions of J_C and J_S with respect to the spin bias, while such asymmetries are absent in antiparallel magnetic configurations. Specifically, for $\varepsilon_\mathrm{d} > 0$, a positive spin bias enhances charge and spin currents, while a negative spin bias suppresses these transport phenomena, demonstrating a robust spin bias-driven diode effect. Notably, such asymmetric distributions can be electrically controlled by tuning the gate voltage. When $\varepsilon_\mathrm{d} < -7$ meV, the currents $|J_{C/S}^+|$ become smaller than $|J_{C/S}^-|$, indicating a complete polarity reversal. This polarity-tunable behavior contrasts sharply with traditional diodes, such as PN junctions, whose fixed polarity is determined during fabrication and cannot be reconfigured, highlighting the potential of this device for reconfigurable spintronic applications.

To elucidate the physical mechanism underlying the reversal of rectification direction in the $\varepsilon_\mathrm{d} < -7$-meV region, in Fig. 3, we present a schematic diagram of electron transport processes near this gate voltage. As previously demonstrated in Fig. 1(e), when the QD energy level ε_d enters the $(0, |V_S|)$ interval, the single-occupancy transport channel becomes activated. In this regime, positive spin bias enables spin-up electrons (majority spins) to occupy the QD's level, while negative spin bias facilitates occupation by spin-down electrons (minority spins), irrespective of electrode magnetism, solely due to spin bias effects. Upon further reduction of gate voltage, spin-up or spin-down electrons become trapped in the QD (see Figs. 3(a) and 3(c)). With continued gate voltage decrease, the double-occupancy transport channel emerges as the dominant conduction pathway. Under positive (negative) spin bias, with a spin-up (spin-down) electron trapped in the QD, Pauli exclusion[69,70] dictates that only spin-down (spin-up) electrons can occupy the double-occupancy channel, shifting the transport window from $(|V_S| > \varepsilon_\mathrm{d} > 0)$ to $(0 > (\varepsilon_\mathrm{d} + U) > -|V_S|)$. Consequently, positive (negative) spin bias drives spin-down (spin-up) electrons from the drain to source, reversing current direction (see Figs. 3(b) and 3(d)). Notably, for ferromagnetic electrodes with parallel magnetization alignment, majority-spin currents ($J_\uparrow$) inherently exceed minority-spin ($J_\downarrow$) contributions. The combined effects of the Pauli exclusion and Coulomb blockade ensure that under

a consistent spin bias direction, carriers transported through the single-occupancy channel and the double-occupancy channel always exhibit opposite spin polarization characteristics. Meanwhile, the dominance of electronic transport by different spin carriers leads to distinct resistance states in parallel configurations. This mechanism ultimately results in the observed reversal of current rectification polarity between two gate voltage regions, as shown in Fig. 2. Similar control mechanisms have been validated and applied in QD-based quantum bit operation.[33,36,48] However, unlike those schemes, the device employs ferromagnetic electrodes for both terminals in the present study.

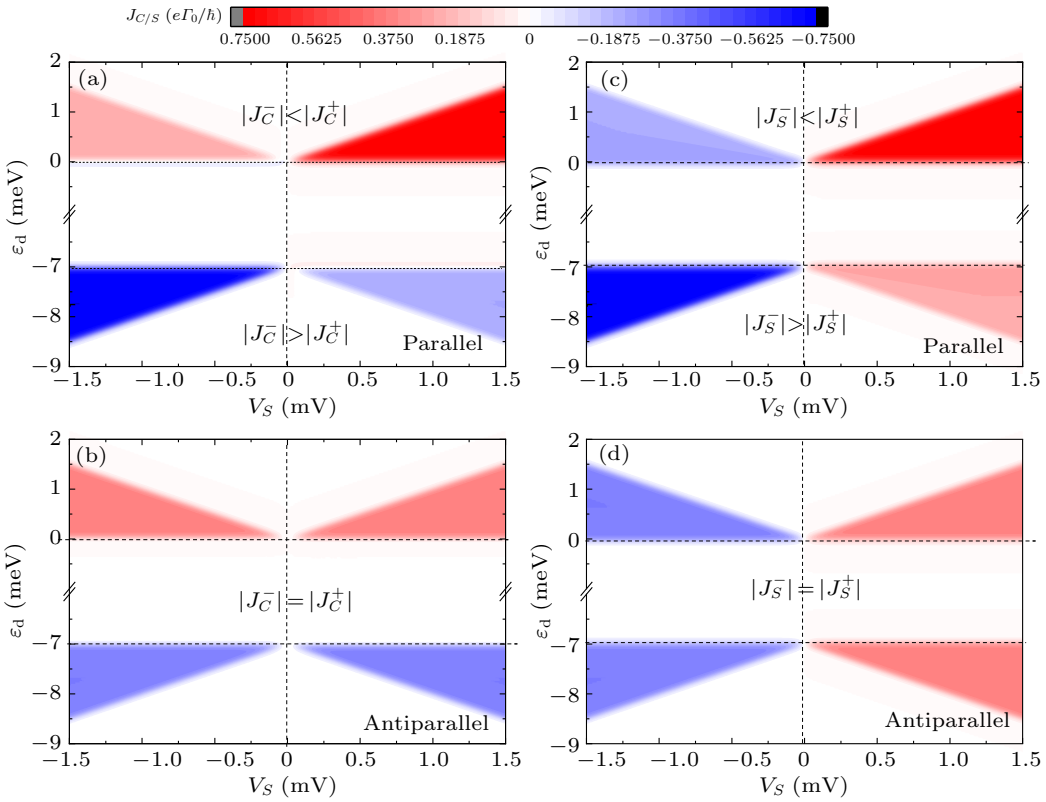


Fig. 2. Charge current [(a) and (b)] and spin current [(c) and (d)] as functions of gate voltage and spin bias under the parameters $T = 1$ K, spin polarization rate $\eta = 0.5$, and Coulomb repulsion $U = 7$ meV, for parallel [(a) and (c)] and antiparallel [(b) and (d)] magnetic configurations.

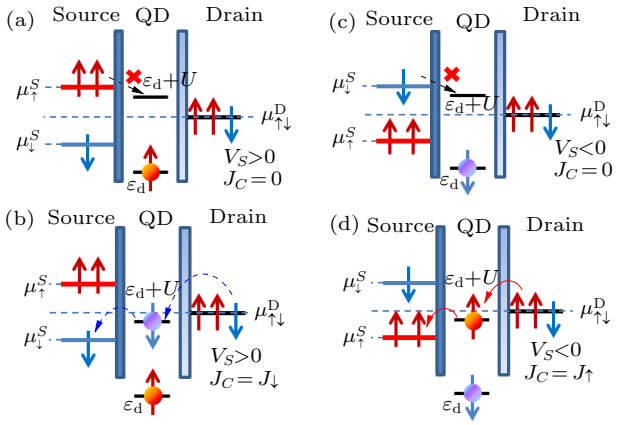


Fig. 3. Electron transport schematics under [(a) and (b)] positive and [(c) and (d)] negative spin bias directions in the parallel configuration. At low gate voltages, a spin-up electron is confined within the QD under positive spin bias [(a) and (b)], while the negative spin bias [(c) and (d)] induces the opposite polarization. Doubly occupied channels dominate the electron transport process in this regime.

4.2. Spin-bias-induced perfect diode effect

To clearly demonstrate the rectification effects within the device, we calculated the charge and spin currents as functions of spin bias V_S at different temperatures for $\varepsilon_d = 0.5$ meV, as shown in Figs. 4(a) and 4(c). We observe that while both $J_{C/S}^+$ and $J_{C/S}^-$ decrease with increasing temperature, the asymmetric distributions of charge and spin currents with respect to V_S persist. Notably, under low temperatures, the spin current reverses its direction with V_S, whereas the charge current remains unidirectional. As the temperature rises, the charge current in Fig. 4(a) gradually develops a "spoon-shaped" asymmetric distribution, with its minimum value slightly dropping below zero in the small negative spin bias region. However, as $|V_S|$ increases further, the current will recover to positive values quickly and then form a small positive J_C plateau.

Figure 4(b) illustrates the dependence of $J_{C/S}^+$ and $J_{C/S}^-$ on the gate voltage. We find that positive ($V_S = +0.5$ mV) and negative ($V_S = -0.5$ mV) spin biases drive electron transport predominantly in two distinct gate voltage regions: $\varepsilon_d \in [-0.5, 1]$ meV and $\varepsilon_d \in [-8, -6.5]$ meV, with opposite rectification polarities in these regions. Intriguingly, unlike the spin current, the charge current vanishes at two specific gate voltages, $\varepsilon_d(\chi^+) \approx 0$ meV and $\varepsilon_d(\chi^-) \approx -7$ meV, indicat-

ing that charge transport is permitted only for a single spin bias direction at these points. As shown in Fig. 4(d), we further analyze the charge current and spin-σ current distributions at these critical points, $\chi^{\pm}$. At $\varepsilon_{\rm d}(\chi^{+})$, a positive spin bias induces a finite charge current, while a negative spin bias generates a pure spin current characterized by counter-propagating spin-up and spin-down currents of equal magnitude through the quantum dot. If we calculate the rectification ratio ($RR = |J_C^{\rm forward}/J_C^{\rm reverse}|$) of the diode at this point, this value should theoretically approach infinity ($RR > 3\times10^6$ when $|V_S| > 1.3$ mV). A similar phenomenon occurs at $\varepsilon_{\rm d}(\chi^{-})$, but with reversed rectification polarity. These results demonstrate that the device exhibits not only polarity-tunable charge current rectification but also achieves perfect rectification at specific gate voltages, where the reverse-bias charge current is entirely suppressed to zero.

As shown in Fig. 4(d), we further analyze the charge current and spin-σ current distributions at these critical points $\chi^{\pm}$. At $\varepsilon_{\rm d}(\chi^{+})$, a positive spin bias induces a finite charge current, while a negative spin bias generates a pure spin current characterized by counter-propagating spin-up and spin-down currents of equal magnitude through the quantum dot. A similar phenomenon occurs at $\varepsilon_{\rm d}(\chi^{-})$, but with the reversed rectification polarity. These results demonstrate that the device exhibits not only polarity-tunable charge current rectification but also achieves perfect rectification at specific gate voltages, where the reverse-bias charge current is entirely suppressed to zero.

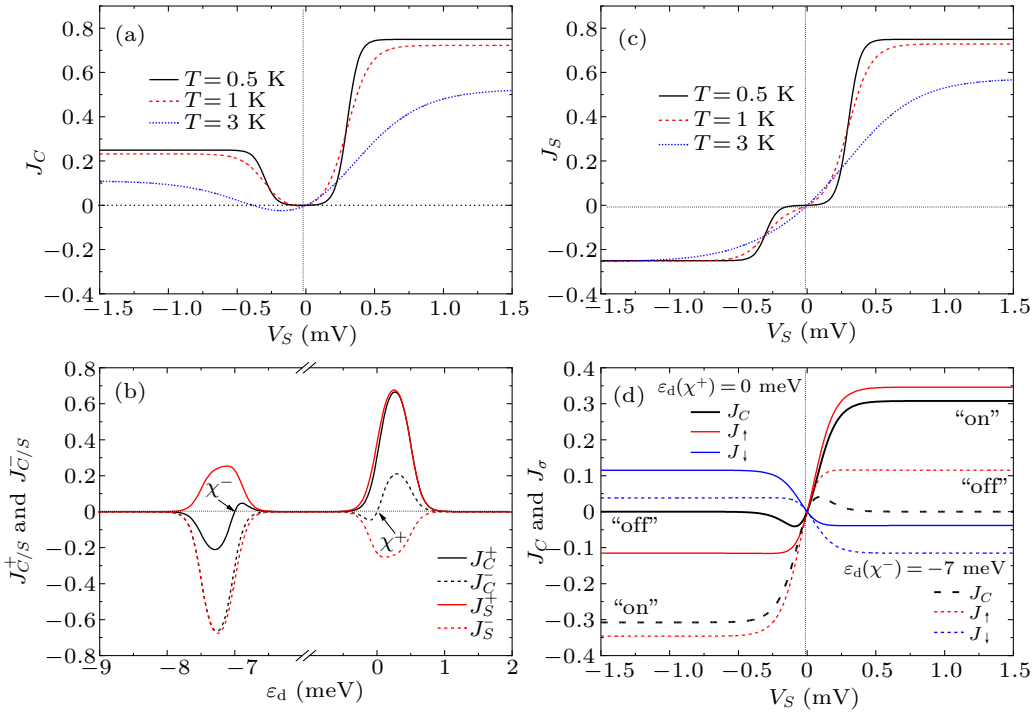


Fig. 4. (a) Charge current and (b) spin current as functions of spin bias V_S at varying temperatures under a fixed gate voltage $\varepsilon_{\rm d} = 0.5$ meV. (c) Gate voltage dependence of charge currents and spin currents under spin bias $V_S = \pm0.5$ mV and temperature $T = 1$ K, where forward charge current J_C^{+} and reverse charge current J_C^{-} exhibit sign reversals near positions χ^{-} and χ^{+}, respectively. (d) Spin bias dependence of charge currents and spin-σ currents at points $\chi^{\pm}$ with temperature $T = 1$ K. Other Parameters are set as: Coulomb repulsion $U = 7$ meV, ferromagnetic electrode polarization $\eta = 0.5$, and system arrange in parallel magnetic configuration.

To investigate the perfect diode effect observed in the charge current at points $\chi^{\pm}$, we calculated the spin-resolved current as a function of gate voltage at $T = 0.2$ K, as shown in Fig. 5(a). Due to the extremely low temperature, electron transport is primarily confined to the energy windows $(0, |V_S|)$ and $(-U, -U - |V_S|)$. When $\varepsilon_{\rm d}$ lies within the $(0, |V_S|)$ region, as anticipated in Figs. 1(b) and 1(c), a positive spin bias drives a significant spin-up (majority) current from the source to the drain, while a negative spin bias induces a smaller spin-down (minority) current in the same direction. At the $\varepsilon_{\rm d}(\chi^{+}) \approx 0$ point (see Fig. 5(e)), the QD energy level aligns with the chemical potential of the D electrode, allowing a small fraction of electrons from the D electrode to tunnel back to the S electrode. This small conductive region rapidly vanishes as the gate voltage decreases, because under the combined action of spin bias and Coulomb blockade, the quantum dot traps a spin-σ electron, thereby completely blocking the transport channel within the QD. As shown in Fig. 5(a), for positive spin bias, the trapped electron is spin-up, and the returning current is spin-down (minority), resulting in $|J_{\uparrow}^{+}| >> |J_{\downarrow}^{+}|$ and a positive charge current. Conversely, for negative spin bias, the trapped electron is spin-down, and the returning electrons are spin-up (majority), leading to a probabilistic simultaneous occurrence of a spin-up (majority) return current and a spin-down (minority) forward current near $\varepsilon_{\rm d} = 0$, finally resulting in a charge-neutral pure spin current near the $\varepsilon_{\rm d} = 0$ regime. It should be

mentioned that this phenomenon can only emerge in parallel configurations. This is because in antiparallel structures, the spin polarizations of the source and drain electrodes are opposite, meaning there is no overall dominance of majority or minority spin carriers in the total system.

To better explain the pure spin current effect under reverse bias occurring at the χ^+ point, we derive an analytical expression for the current near $\varepsilon_d \to 0$ under certain approximate conditions. Assuming the system satisfies $U > |V_S| \gg |\varepsilon_d|$ and k_BT, the current expression in this region can be approximated based on formulas from Refs. [66,67] as

$$J_C^+ \approx \Lambda\left[\exp\left(\frac{\varepsilon_d}{k_BT}\right)(\eta+1)+\eta\right],$$
$$J_C^- \approx -\Lambda\left[\exp\left(\frac{\varepsilon_d}{k_BT}\right)(\eta-1)+\eta\right], \tag{6}$$

where

$$\Lambda = \frac{2\exp\left(\varepsilon_d/k_BT\right)}{2+7\exp\left(\varepsilon_d/k_BT\right)+4\exp\left(2\varepsilon_d/k_BT\right)}.$$

Clearly, regardless of variations in ε_d and η, the forward current J_C^+ in this region is always greater than zero, whereas the reverse current J_C^- can drop to zero depending on changes in ε_d and η. Furthermore, since the magnitude of the reverse current J_C^- depends on factor $\exp\left[\varepsilon_d/k_BT\right](\eta-1)+\eta$, we expand J_C^- in a Taylor series:

$$J_C^- \approx -\Lambda\left[(2\eta-1)+\frac{\varepsilon_d(\eta-1)}{k_BT}+\frac{\varepsilon_d^2(\eta-1)}{(k_BT)^2}+\mathcal{O}(\varepsilon_d)^3\right]. \tag{7}$$

From this expansion, we observe that: (i) when the spin polarization rate is $\eta = 0.5$, the current reaches zero if and only if $\varepsilon_d = 0$; (ii) when η exceeds 0.5, the zero point of the reverse current χ^+ shifts toward $\varepsilon_d > 0$ direction; (iii) when $\eta < 0.5$, the χ^+ shifts toward $\varepsilon_d < 0$ direction. This solution is highly consistent with the positional changes of χ^+ observed in Figs. 4 and 5(b), providing a clear explanation for the physical origin of the perfect diode effect near the $\varepsilon_d \to 0$ regime. Moreover, under the same approximate conditions, we derive the expression for the reverse spin current near $\varepsilon_d \to 0$

$$J_S^- \approx \Lambda\left[\exp\left(\frac{\varepsilon_d}{k_BT}\right)(\eta-1)-\eta\right]. \tag{8}$$

Clearly, regardless of how η and ε_d vary, the spin current under reverse bias cannot reach zero. This is precisely the physical origin of the pure spin current effect at point χ^+ under reverse bias.

The pure spin current at point χ^- originates from a similar mechanism in which the electron transport process is dominated by the doubly occupied channel $(\varepsilon_d + U)$. However, as we have discussed in Fig. 3, the interplay between Pauli exclusion and Coulomb repulsion preferentially facilitates the tunneling of spin-down electrons in a positive spin bias direction, thereby suppressing the current in the $V_S > 0$ regime. As a result, a pure spin current phenomenon emerges near $\varepsilon_d \approx -7$ meV under the $V_S > 0$ direction, which corresponds to $J_\uparrow^+ = -J_\downarrow^+$ at the χ^- point.

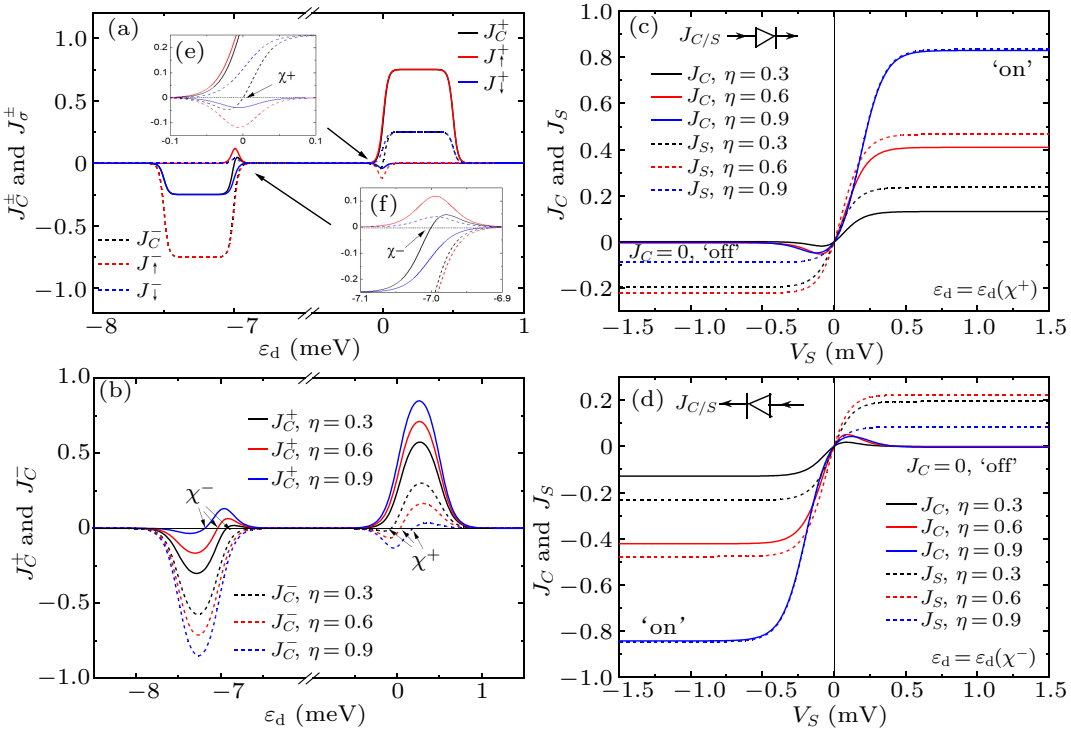


Fig. 5. (a) Gate voltage dependence of forward (or reverse) charge currents and spin-σ currents under a low temperature $T = 0.2$ K. (b) Gate voltage dependence of forward and reverse charge currents at $T = 1$ K, under different ferromagnetic polarization η. (c)–(d) Spin bias dependence of charge and spin currents at the specific points χ^+ (c) and χ^- (d) with different ferromagnetic polarization η. The inserted figures (e) and (f) illustrate the distributions of spin$-\sigma$ currents and charge current near $\chi^\pm$ points.

Figures 5(c) and 5(d) present the charge and spin currents at the χ^+ and χ^- points for different electrode polarization η. Notably, the rectification directions for charge and spin currents at χ^+ and χ^- are completely opposite. Although enhancing the polarization of the ferromagnetic electrodes boosts the 'on'-state charge current, the reverse-bias current remains consistently suppressed to zero independent of the polarization level. This demonstrates that through gate voltage modulation, the device can always access specific operational regimes achieving perfect current rectification, with this behavior being independent of ferromagnetic electrodes requiring high spin polarization.

4.3. Spin-bias-induced magneto-resistance effect

While the parallel configuration exhibits rectification effects for both charge and spin currents, such behavior is absent in the antiparallel configuration. As shown in Figs. 2(b) and 2(d), the distributions of J_C and J_S with respect to V_S remain symmetric regardless of the gate voltage. To discuss the TMR ratio in the system, it is necessary to contrast the charge currents in parallel and antiparallel configurations. In Fig. 6(a), we calculated the charge current distributions for gate voltages away from the $\chi^\pm$ point. Notably, the "spoon-shaped" asymmetric distribution is exclusive to the parallel configuration, while the antiparallel configuration maintains symmetric current distributions. Moreover, when $\varepsilon_d \in (0, |V_S|)$, the currents satisfy $|J_P^+| > |J_{AP}^+| = |J_{AP}^-| > |J_P^-|$, indicating that NMR phenomena occur in the $V_S < 0$ region. Similarly, when ε_d falls within the $(-U, -U-|V_S|)$ interval, the current hierarchy shifts to $|J_P^-| > |J_{AP}^-| = |J_{AP}^+| > |J_P^+|$, implying NMR occurs in the $V_S > 0$ region. Figure 6(c) presents the temperature-dependent magnetoresistance under these gate voltage conditions. The TMR distribution can be divided into four regions: (I) $\varepsilon_d \in (0, |V_S|)$ and $V_S > 0$, (II) $\varepsilon_d \in (-U, -U-|V_S|)$ and $V_S < 0$, (III) $\varepsilon_d \in (0, |V_S|)$ and $V_S < 0$, and (IV) $\varepsilon_d \in (-U, -U-|V_S|)$ and $V_S > 0$. NMR effects are observed in regions (III) and (IV). Interestingly, as $|V_S|$ increases, the TMR value converges to two distinct values: in regions (I) and (II), positive TMR approaches $+1$, while in regions (III) and (IV), it tends toward -0.335. Furthermore, we observe that elevated temperatures significantly influence the magnetoresistance in the small spin bias regime. However, the influence of temperature on the TMR gradually diminishes with increasing $|V_S|$ and finally becomes negligible in the high spin bias regime.

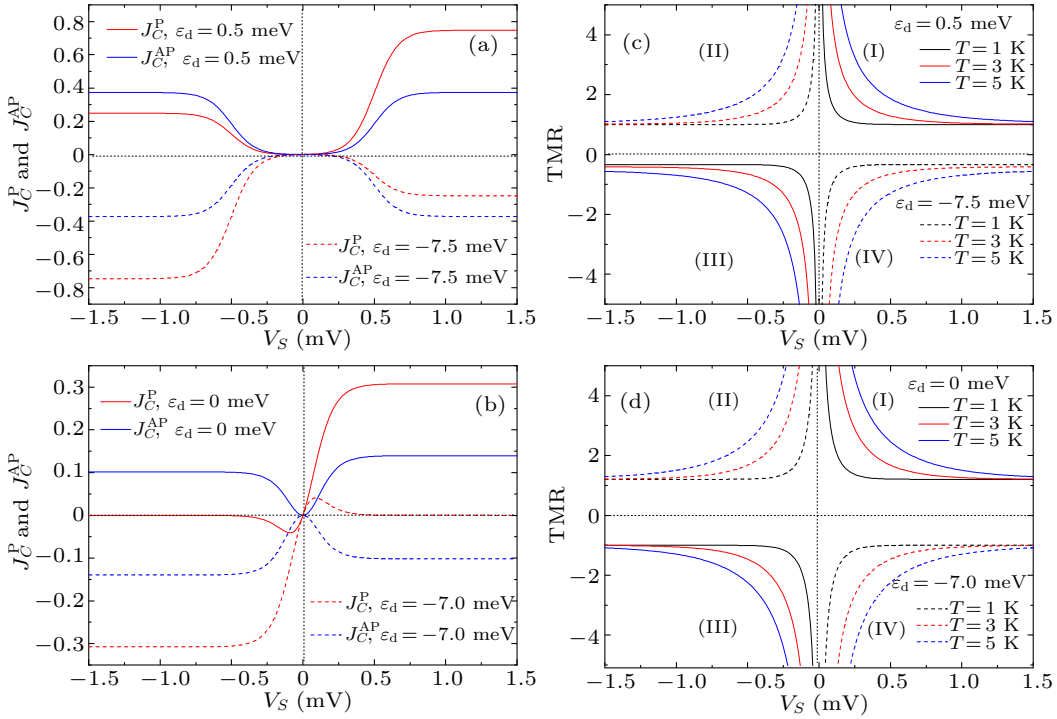


Fig. 6. (a) Charge current *versus* spin bias V_S in parallel and antiparallel configurations at gate voltages $\varepsilon_d = 0.5$ meV and -7.5 meV; (b) Corresponding behavior at critical gate voltages $\varepsilon_d(\chi^+) = 0$ meV and $\varepsilon_d(\chi^-) = -7$ meV, with temperature $T = 1$ K. The on-off ratio under spin bias $V_S = -1.2$ mV is $J_{AP}/J_P \approx 1.1 \times 10^6$. (c) Tunneling magnetoresistance *versus* V_S for $\varepsilon_d = 0.5$ meV and -7.5 meV; (d) TMR response at critical voltages $\varepsilon_d(\chi^+) = 0$ meV and $\varepsilon_d(\chi^-) = -7$ meV, at different equilibrium temperatures. Other parameters are set as $U = 7$ meV and $\eta = 0.5$.

In panels 6(b) and 6(d), we calculated the parallel/antiparallel currents and their TMR distributions when the gate voltage is set at the $\chi^\pm$ points. Due to the perfect rectification effect of the parallel configuration on charge current, the antiparallel-to-parallel current on/off ratio can reach up to 10^6 and the negative TMR value almost approaches -1 under a large spin bias. This indicates that in these parameter regions, only the antiparallel configuration allows current transport, while the net charge transport in the parallel configuration vanishes. Analogously, while the TMR ratios in

low spin bias regimes exhibit significant temperature dependence, we observe that when the spin bias magnitude exceeds a critical threshold ($|V_S| > 1.5$ mV, $\Delta\mu^S > 3$ meV, as shown in Fig. 6(d)), all temperature-dependent negative TMR values converge rapidly toward the theoretical limit of -1. This robust saturation behavior demonstrates that enhanced spin bias effectively suppresses thermal disturbances, enabling reliable experimental observation of the negative TMR phenomenon without requiring cryogenic stabilization.

It is important to note that, according to the definition of TMR in Eq. (5), as temperature increases, we observe a significant distribution of TMR < -1 in regions with $|V_S| \to 0$ (see Figs. 6(b) and 6(d)). By comparing with Fig. 3(a), we find that this phenomenon arises because increasing temperature causes the direction of the charge current to reverse in the small $|V_S|$ regime. In this case, while the absolute value of the parallel current is not zero, the TMR value becomes smaller than -1 due to the sign switch of $J_{\rm P}$. Given that experimental measurements predominantly focus on the absolute current magnitudes in parallel and antiparallel configurations, TMR $= -1$ corresponds to the most anomalous NMR effect. This extreme value arises from the complete suppression of current in the parallel configuration ($J_{\rm P} = 0$) while maintaining finite antiparallel conduction ($|J_{\rm AP}| > 0$), leading to a theoretically infinite current switching ratio $J_{\rm AP}/J_{\rm P} \to \infty$.

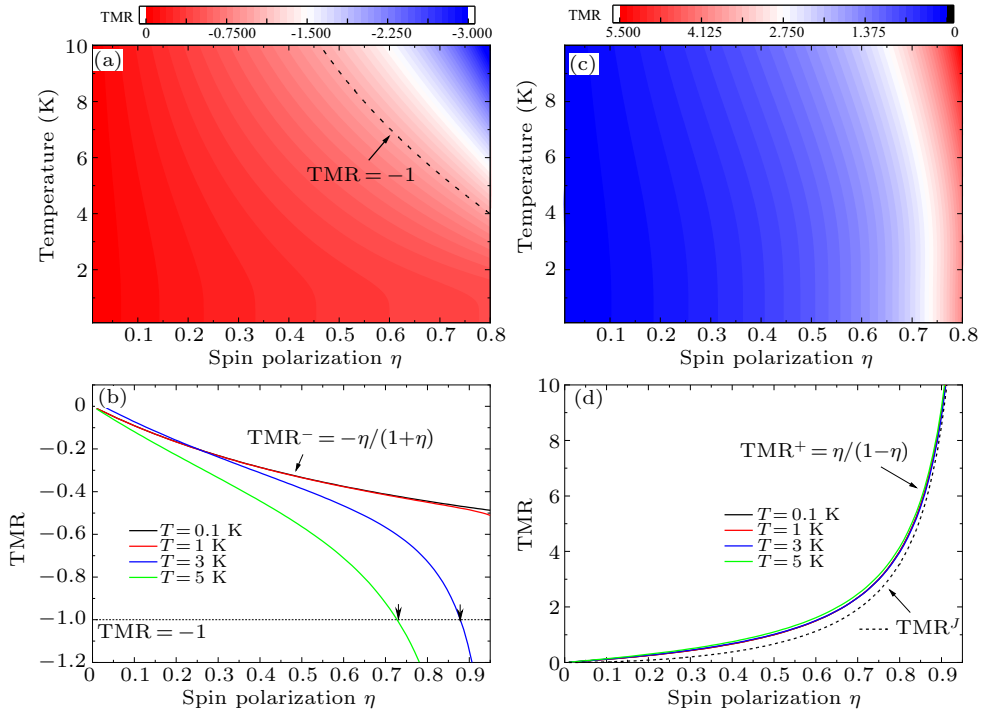


Fig. 7. TMR as functions of spin polarization η and equilibrium temperature T with $V_S = -1.5$ mV, (a) $\varepsilon_{\rm d} = 0.5$ meV and (c) $\varepsilon_{\rm d} = -7.5$ meV. (b) TMR *versus* η with $\varepsilon_{\rm d} = 0.5$ meV and (d) $\varepsilon_{\rm d} = -7.5$ meV at different temperatures, demonstrating thermally controlled spin-resolved electron transport.

In Fig. 7, we investigate the relationship between the tunneling magnetoresistance and the polarization parameter η of the ferromagnetic electrodes. Figures 7(a) and 7(c) depict the TMR distributions as functions of the ferromagnetic polarization η and temperature T at $V_S = -1.5$ mV for $\varepsilon_{\rm d} = 0.5$ meV and $\varepsilon_{\rm d} = -7.5$ meV, respectively. Regardless of variations in the polarization rate, the TMR remains consistently negative in Fig. 7(a) and persistently positive in Fig. 7(c). Interestingly, in Fig. 7(a), we identify a distinct curve (dashed line) where all TMR values equal -1. This curve delineates the distribution of χ^+ points under varying electrode polarization and equilibrium temperature. This indicates that the positions of the critical points χ^+ (or χ^-) are not solely determined by the electrode polarization η but are also significantly influenced by temperature T. To validate this, we calculate the TMR distributions as functions of polarization η for four different temperatures in Fig. 7(c). At lower temperatures, the negative TMR gradually decreases below zero with increasing polarization but fails to reach the limit value of TMR $= -1$. However, at elevated temperatures, the NMR effect is amplified, enabling the TMR to attain -1 at a sufficiently large polarization parameter without altering the gate voltage, thereby inducing perfect current rectification and a giant on-off ratio $J_{\rm AP}/J_{\rm P}$. In contrast to the NMR phenomenon, the positive TMR in Fig. 7(b) appears minimally affected by temperature and increases monotonically with polarization. As shown in Fig. 7(d), we compute the positive TMR distributions as functions of η for multiple temperatures. We observe that the positive TMR curves under a larger bias voltage ($|V_S| = 1.5$ mV) are nearly temperature-independent and consistently exceed the classical Jullière model predictions. By analyzing the electron transport properties at $T = 0$ K, we derive the analyti-

cal expressions for negative TMR ($\mathrm{TMR}^- = -\eta/(1+\eta)$) and positive TMR ($\mathrm{TMR}^+ = \eta/(1-\eta)$). These expressions align closely with the low-temperature TMR profiles in Fig. 7 and rationalize why TMR^+ always surpasses the TMR value predicted by the Julli*è*re model ($\mathrm{TMR}^J = 2\eta^2/(1-\eta^2)$). Notably, at higher temperatures, the NMR effect exhibits pronounced sensitivity to ambient temperature, suggesting that thermal conditions may serve as an additional tunable parameter for modulating current switching ratios and rectification efficiency in such devices.

Finally, we discuss the experimental feasibility of the proposed device. According to references,[56,57] a spin accumulation $\Delta\mu$ on the order of 4 meV–10 meV can be achieved in the source electrode using two-dimensional materials. This demonstrates that the range of spin bias applied in our proposal is experimentally achievable. Although our model does not explicitly include various spin-flip mechanisms, such as those arising from spin–orbit interactions, the results of *R*. Jansen *et al*. demonstrated that spin accumulation and spin bias strongly suppress spin-flip processes both within the quantum dot and in the electrodes.[48] Moreover, the use of silicon or graphene-based FM electrodes is highly advantageous, as these materials offer spin relaxation times on the order of seconds and spin diffusion lengths reaching several micrometers at cryogenic temperatures.[72,73] These properties ensure that substantial spin accumulation can be generated and sustained over device-relevant length scales, thereby further suppressing spin relaxation and ensuring operational robustness. Additionally, the tunnel coupling strength adopted in this work is set to $\Gamma_0 \approx 0.01$ meV, yielding a current amplitude on the order of $e\Gamma_0/\hbar \sim 2$ nA, which is readily detectable using standard measurement techniques. In contrast to previous studies of the Kondo effect in quantum dot devices,[74–76] which typically require a coupling strength greater than 0.1 meV and temperatures below 1 K, the combination of weak coupling and the relatively high operating temperatures employed in our calculations makes it reasonable to neglect Kondo correlations in electron transport. All parameter values used here are well within reach of existing experimental capabilities, demonstrating that the device concept proposed in this work is experimentally feasible.

5. Conclusion

In summary, we have theoretically investigated the charge and spin transport properties of a QD-based spin valve device driven by spin bias. Our calculations reveal that in the parallel magnetic configuration, both charge and spin currents through the QD exhibit rectification effects, which can be modulated by the gate voltage applied to the QD. However, such rectification is absent in the antiparallel configuration, leading to gate-tunable magnetoresistance, including the emergence of negative magnetoresistance effects. Notably, in specific gate voltage regimes, the parallel configuration achieves perfect diode rectification, where the forward current is enhanced while the reverse current is completely suppressed to zero. Correspondingly, the magnetoresistance data exhibit a significant negative value (TMR $= -1$), indicating that charge transport is only permitted in the antiparallel configuration, whereas the parallel configuration exclusively supports pure spin current. These findings highlight the potential of spin-bias-driven QD devices for advancing spintronic applications by offering tunable rectification and magnetoresistance functionalities.

Acknowledgements

Project supported by National Natural Science Foundation of China (Grant No. 11404322) and the Natural Science Foundation of Huai'an (Grant No. HAB202229).

References

[1] Žutić I, Fabian J and Sarma S D 2004 *Rev. Mod. Phys.* **76** 323
[2] Pulizzi F 2012 *Nat. Mater.* **11** 367
[3] Xiao J Q, Jiang J S and Chien C L 1992 *Phys. Rev. Lett.* **68** 3749
[4] Sinova J, Valenzuela S O, Wunderlich J, Back C H and Jungwirth T 2015 *Rev. Mod. Phys.* **87** 1213
[5] Ramaswamy R, Lee J M, Cai K and Yang H 2018 *Appl. Phys. Rev.* **5** 031107
[6] Mostufa S, Liang S, Chugh V K, Wang J P and Wu K 2024 *npj Spintronics* **2** 26
[7] Leitao D C, van Riel F J F, Rasly M, Araujo P D R, Salvador M, Paz E and Koopmans B 2024 *npj Spintronics* **2** 54
[8] Železný J, Wadley P, Olejník K, Hoffmann A and Ohno H 2018 *Nat. Phys.* **14** 220
[9] Sun D L, Yin L F, Sun C J, Guo H W, Gai Z, Zhang X G, Ward T Z, Cheng Z H and Shen J 2010 *Phys. Rev. Lett.* **104** 236602
[10] Cardoso C, Soriano D, García-Martínez N A and Fernández-Rossier J 2018 *Phys. Rev. Lett.* **121** 067701
[11] Worledge D C and Hu G H 2024 *Nat. Rev. Electr. Eng.* **1** 730
[12] Xu H W, Wang H, Zhou J and Li J 2021 *Nat. Commun.* **12** 4330
[13] Liu C J, Luo Y M, Hong D S, Zhang S S L, Saglam H, Li Y, Lin Y L, Fisher B, Pearson J E, Jiang J S, Zhou H, Wen J, Hoffmann A and Bhatta-charya A 2021 *Sci. Adv.* **7** 1669
[14] Safranski C, Barsukov I, Lee H K, Schneider T, Jara A A, Smith A, Chang H, Lenz K, Lindner J, Tserkovnyak Y, Wu M and Krivorotov I N 2017 *Nat. Commun.* **8** 117
[15] Uchida K, Takahashi S, Harii K, Ieda J, Koshibae W, Ando K, Maekawa S and Saitoh E 2008 *Nature* **455** 778
[16] Naka M, Motome Y and Seo H 2021 *Phys. Rev. B* **103** 125114
[17] Abdelwahab I, Kumar D, Bian T, Zheng H N, Gao H, Hu F R, McClelland A, Leng K, Wilson W L and Loh K P 2024 *Science* **385** 311
[18] Strambini E, Spies M, Ligato N, Ilić S, Rouco M, González-Orellana C, Ilyn M, Rogero C, Bergeret F S, Moodera J S, Virtanen P, Heikkilä T T and Giazotto F 2022 *Nat. Commun.* **13** 2431
[19] Nadeem M, Fuhrer M S and Wang X L 2023 *Nat. Rev. Phys.* **5** 558
[20] Eisenstein J P, Pfeiffer L N and West K W 2017 *Phys. Rev. Lett.* **118** 186801
[21] Balachandran V, Benenti G, Pereira E, Casati G and Poletti D 2018 *Phys. Rev. Lett.* **120** 200603
[22] Merchant C A and Markovic N 2008 *Phys. Rev. Lett.* **100** 156601
[23] Iovan A, Andersson S, Naidyuk Y G, Vedyaev A, Dieny B and Korenivski V 2008 *Nano Lett.* **8** 805
[24] Sasioğlu E, Aull T, Kutschabsky D, Blügel S and Mertig I 2020 *Phys. Rev. Appl.* **14** 014082
[25] Manipatruni S, Nikonov D E and Young I A 2018 *Nat. Phys.* **14** 338
[26] Chang F J, Lin J G and Huang S Y 2017 *Phys. Rev. Mater.* **1** 031401
[27] Barts E, Tenzin K and Sławińska J 2025 *Nat. Commun.* **16** 4056

[28] Seki S, Ideue T, Kubota M, Kozuka Y, Takagi R, Nakamura M, Kaneko Y, Kawasaki M and Tokura Y 2015 *Phys. Rev. Lett.* **115** 266601
[29] Han W, Maekawa S and Xie X C 2020 *Nat. Mater.* **19** 139
[30] Sun Q F and Xie X C 2015 *Appl. Phys. Lett.* **106** 182407
[31] Zheng J, Chi F and Guo Y 2018 *Appl. Phys. Lett.* **113** 112404
[32] Bo R, Zhang Z Z, Tang Y, Guo Y and Liu H 2023 *Appl. Phys. Express* **16** 083001
[33] Chi F and Sun Q F 2010 *Phys. Rev. B* **81** 075310
[34] Vandersypen L M K, Bluhm H, Clarke J S, Dzurak A S, Ishihara R, Morello A, Reilly D J, Schreiber L R and Veldhorst M 2017 *npj Quantum Inf.* **3** 34
[35] Fedorov P, Soldatov I, Neu V, Schäfer R, Schmidt O G and Karnaushenko D 2024 *Nat. Commun.* **15** 2048
[36] Ciriano-Tejel V N, Fogarty M A, Schaal S, Hutin L, Bertrand B, Ibberson L, Gonzalez-Zalba M F, Li J, Niquet Y M, Vinet M and Morton J J L 2021 *PRX Quantum* **2** 010353
[37] Burkard G, Ladd Th D, Pan A, Nichol J M and Petta J R 2023 *Rev. Mod. Phys.* **95** 025003
[38] Manchon A, Železny J, Miron I M, Jungwirth T, Sinova J, Thiaville A, Garello K and Gambardella P 2019 *Rev. Mod. Phys.* **91** 035004
[39] Hanson R, Kouwenhoven L P, Petta J R, Tarucha S and Vandersypen L M K 2007 *Rev. Mod. Phys.* **79** 1217
[40] Hensen B, Huang W W, Yang C H, Chan K W, Yoneda J, Tanttu T, Hudson F E, Laucht A, Itoh K M, Ladd T D, Morello A and Dzurak A S 2020 *Nat. Nanotechnol.* **15** 13
[41] Stano P, Fabian J and Jacquod P 2012 *Phys. Rev. B* **85** 241301(R)
[42] Yang Z C, Sun Q F and Xie X C 2014 *J. Phys.: Condens. Matter* **26** 045302
[43] Ramos E, Silva-Valencia J, Franco R, Siqueira E C and Figueira M S 2015 *Physica E* **74** 334
[44] Jansen R, Spiesser A, Saito H, Fujita Y, Yamada S, Hamaya K and Yuasa S 2018 *Phys. Rev. Appl.* **10** 064050
[45] Vera-Marun I J, Ranjan V and van Wees B J 2012 *Nat. Phys.* **8** 313
[46] van 't Erve O M J, Friedman A L, Cobas E, Li C H, Robinson J T and Jonker B T 2012 *Nat. Nanotechnol.* **7** 737
[47] Sierra J F, Neumann I, Cuppens J, Raes B, Costache M V and Valenzuela S O 2018 *Nat. Nanotechnol.* **13** 107
[48] Jansen R and Yuasa S 2024 *npj Quantum Inf.* **10** 21
[49] Jansen R and Yuasa S 2024 *Phys. Rev. Appl.* **22** 054049
[50] Jansen R and Yuasa S 2025 *Phys. Rev. B* **111** 104407
[51] Bloom F L, Wagemans W, Kemerink M and Koopmans B 2007 *Phys. Rev. Lett.* **99** 257201
[52] Alekseev P S 2016 *Phys. Rev. Lett.* **117** 166601
[53] Dai X, Du Z Z and Lu H Z 2017 *Phys. Rev. Lett.* **119** 166601
[54] Blonski P, Tucek J, Sofer Z, Mazanek V, Petr M, Pumera M, Otyepka M and Zboril R 2017 *J. Am. Chem. Soc.* **139** 3171
[55] Tokmachev A M, Averyanov D V, Parfenov O E, Taldenkov A N, Karateev I A, Sokolov I S, Kondratev O A and Storchak V G 2018 *Nat. Commun.* **9** 1672
[56] Gurram M, Omar S and van Wees B J 2017 *Nat. Commun.* **8** 248
[57] Spiesser A, Saito H, Fujita Y, Yamada S, Hamaya K, Yuasa S and Jansen R 2017 *Phys. Rev. Appl.* **8** 064023
[58] Xu Z Y, Wang J L, Pan Y H, Lv B, Zhu Y L, Wu Z H and Dai Y H 2025 *Appl. Phys. Lett.* **127** 093101
[59] Liu Z, Abe S, Shimizu M and Yugami H 2023 *Appl. Phys. Lett.* **122** 093502
[60] Liu P, Niu W, Li Y D, Hou D, Sheng Z G, Zhu H P, Mao W W, Luo H C, Zhou S and Pu Y 2024 *Appl. Phys. Lett.* **124** 091901
[61] Ikeda S, Hayakawa J, Ashizawa Y, Lee Y M, Miura K, Hasegawa H, Tsunoda M, Matsukura F and Ohno H 2008 *Appl. Phys. Lett.* **93** 082508
[62] Liu R R, Zhou J M, Zhang R, Yuan H, Liao X X, Zhou Y B, He J J and Yuan J R 2025 *Appl. Phys. Lett.* **126** 222403
[63] Jeong J W, Filippou C F, Ferrante Y, Garg C, Ikhtiar T T, Yang S H, Parkin S P and Samant M G 2025 *Appl. Phys. Lett.* **126** 252402
[64] Rejec T, Žitko R, Mravlje J and Ramšak A 2012 *Phys. Rev. B* **85** 085117
[65] Mazal Y, Meir Y and Dubi Y 2019 *Phys. Rev. B* **99** 075433
[66] Qi F H, Ying Y B and Jin G J 2011 *Phys. Rev. B* **83** 075310
[67] Souza F M, Egues J C and Jauho A P 2007 *Phys. Rev. B* **75** 165303
[68] van der Wiel W G, De Franceschi S, Elzerman J M, Fujisawa T, Tarucha S and Kouwenhoven L P 2002 *Rev. Mod. Phys.* **75** 1
[69] Ono K, Austing D G, Tokura Y and Tarucha S 2002 *Science* **297** 1313
[70] Johnson A C, Petta J R, Marcus C M, Hanson M P and Gossard A C 2005 *Phys. Rev. B* **72** 165308
[71] Julliere M 1975 *Phys. Lett. A* **54** 225
[72] Simmons C B, Prance J R, Van Bael B J, Koh T S, Shi Z, Savage D E, Lagally M G, Joynt R, Friesen M, Coppersmith S N and Eriksson M A 2011 *Phys. Rev. Lett.* **106** 156804
[73] Gachter L M, Garreis R, Tong C, Kratochwi B, Gerber J D, Folkert Kornelis de Vries, Ruckriegel M J, Watanabe K, Takashi T, Ihn T, Ensslin K, Kurzmann A and Huang W W 2022 *Phys. Rev. X Quantum* **3** 020343
[74] Jeong H, Chang A M and Melloch M R 2001 *Science* **293** 2221
[75] Gaass M, Hüttel A K, Kang K, Weymann I, von Delft J and Strunk Ch 2011 *Phys. Rev. Lett.* **107** 176808
[76] Cronenwett S M, Oosterkamp T H and Kouwenhoven L P 1998 *Science* **281** 540